ADVANCED FUNCTIONAL MATERIALS
www.afm-journal.de

Harnessing Anti-Parity-Time Phase Transition in Coupled Topological Photonic Valley Waveguides

Xinrong Xie, Maoliang Wei, Yumeng Yang, Yuanzhen Li, Kunhao Lei, Zijian Zhang, Chi Wang, Chuyu Zhong, Lan Li, Zuojia Wang, Wei E. I. Sha, Erping Li, Haoran Xue, Zhaoju Yang, Luqi Yuan, Hongsheng Chen, Hongtao Lin,* and Fei Gao**

Topological and non-Hermitian physics provide powerful tools for manipulating light in different ways. Recently, intense studies have converged on the interplay between topology and non-Hermiticity, and have produced fruitful results in various photonic settings. Currently, the realization of this interplay falls under the paradigm of enabling energy exchange between topological systems and the environment. Beyond this paradigm, it is revealed that a non-Hermitian phenomenon, i.e., the anti-parity-time phase transition, naturally emerges from a Hermitian system realized by coupled topological valley waveguides. Such phase transition gives two exotic topological superstates in the spectral domain. By further combining the two phases with topological robustness, a photonic topological bi-functional device is realized on a silicon-on-insulator platform at telecommunications frequencies. The results provide a new perspective on light manipulation and integrated device applications.

1. Introduction

Discovering distinctive phases is a recurring theme in research on natural and artificial materials, and lays the foundation for disruptive technological applications. To understand the distinct properties of material phases, theories of phase transitions based on topology changes and symmetry breaking have been well developed.[1] Decades ago, topological properties[2,3] and parity–time (PT) symmetry[4] were introduced into photonics in parallel and have ignited intensive attention on topological photonics[5] and non-Hermitian photonics,[6,7] respectively. These two fields offer fascinating light-manipulation approaches in different ways.[5–7] More specifically, the most striking property of a

X. Xie, M. Wei, Y. Yang, Y. Li, K. Lei, Z. Zhang, C. Wang, C. Zhong, Z. Wang, W. E. I. Sha, E. Li, Z. Yang, H. Chen, H. Lin, F. Gao
Interdisciplinary Center for Quantum Information
State Key Laboratory of Extreme Photonics and Instrumentation
ZJU-Hangzhou Global Scientific and Technological Innovation Center
Zhejiang University
Hangzhou 310027, China
E-mail: hansomchen@zju.edu.cn; hometown@zju.edu.cn; gaofeizju@zju.edu.cn

X. Xie, M. Wei, Y. Yang, Y. Li, K. Lei, Z. Zhang, C. Wang, C. Zhong, Z. Wang, W. E. I. Sha, E. Li, H. Chen, H. Lin, F. Gao
International Joint Innovation Center
The Electromagnetics Academy at Zhejiang University
Zhejiang University
Haining 314400, China

X. Xie, M. Wei, Y. Yang, Y. Li, K. Lei, Z. Zhang, C. Wang, C. Zhong, Z. Wang, H. Chen, H. Lin, F. Gao
Key Lab. of Advanced Micro/Nano Electronic Devices & Smart Systems of Zhejiang
Jinhua Institute of Zhejiang University
Zhejiang University
Jinhua 321099, China

X. Xie, M. Wei, Y. Yang, Y. Li, K. Lei, Z. Zhang, C. Wang, C. Zhong, Z. Wang, H. Chen, H. Lin, F. Gao
Shaoxing Institute of Zhejiang University
Zhejiang University
Shaoxing 312000, China

L. Li
Key Laboratory of 3D Micro/Nano Fabrication and Characterization of Zhejiang Province
School of Engineering
Westlake University
Hangzhou 310024, China

H. Xue
Division of Physics and Applied Physics
School of Physical and Mathematical Sciences
Nanyang Technological University
Singapore 637371, Singapore

Z. Yang
Department of Physics
Zhejiang University
Hangzhou 310027, China

L. Yuan
State Key Laboratory of Advanced Optical Communication Systems and Networks
School of Physics and Astronomy
Shanghai Jiao Tong University
Shanghai 200240, China

The ORCID identification number(s) for the author(s) of this article can be found under https://doi.org/10.1002/adfm.202302197

DOI: 10.1002/adfm.202302197

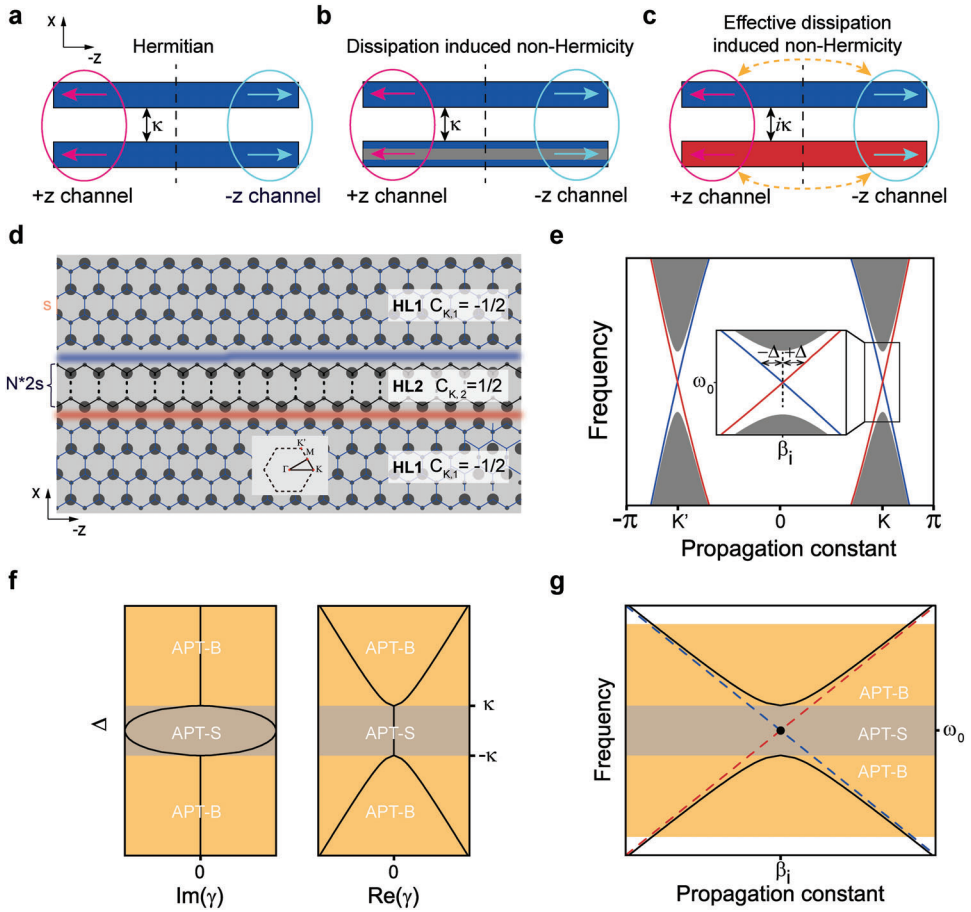

Figure 1. Hermitian-topology-spawned APT symmetry. a–c) Model comparison for elucidating the effective dissipation in coupled waveguides. The blue/red rectangles indicate forward-wave/backward-wave waveguides (FWG/BWG). (a), (b), and (c) show lossless FWG-FWG, lossy FWG-FWG, and FWG-BWG models, respectively. The arrows depict the mode propagation direction of the mode in the coupled waveguides. κ and $i\kappa$ are the coupling factors. The gray in (b) and the mode propagating along the $+z$ channel in (c) represent the practical and effective dissipation, respectively. d) Two topological interfaces (HL1-HL2 and HL2-HL1) for realizing the FWG and BWG. The two honeycomb lattices (HL1 and HL2) share the same Brillouin zone (inset) but exhibit opposite valley Chern numbers C_K. The distances between the nearest atoms and interfaces are s and $N \times 2s$ ($N \in Z^+$), respectively. e) The blue/red linear dispersions correspond to the upper/lower interfaces in (d). With respect to the intersection point (K, ω_0), their wavevectors are oppositely detuned by $\pm\Delta$. The CTVWs give an effective Hamiltonian $\hat{H}_{\text{eff}} = \begin{bmatrix} -\Delta & i\kappa \\ i\kappa & \Delta \end{bmatrix}$, respecting APT symmetry. f) Spontaneous APT symmetry breaking in CTVWs. γ denotes the eigenvalues of H_{eff}. g) Dispersion relations of the CTVWs (black solid line), individual FWG (red dashed line), and BWG (blue dashed line). The brown/orange region corresponds to the APT-S/APT-B phase.

topological system is its robust edge/interface states that are resilient to structural imperfections,[8–11] enabling applications in robust optoelectronic devices,[5] while a system respects PT symmetry, exhibiting non-Hermitian phase transitions,[6,7] provides fascinating approaches for manipulating light strengths or spectral line shapes.[6,7] The recently emerging anti-parity-time (APT) symmetry has also attracted much attention,[12–32] and resulted in interesting applications, e.g., mode switching,[18,32] optical routers,[24] and ultrasensitive sensing.[20,26,28]

Recently, intense studies have converged on the interplay between topology and non-Hermiticity,[33–35] and have discovered exotic non-Hermitian topological phases in various photonic settings. These phases bring fascinating consequences ranging from intriguing phenomena, for example, non-Hermitian topological light steering,[36] funneling,[37] and nonlinear tuning,[38] to technological applications, such as topological lasing.[39,40] The construction of these settings mainly falls under the paradigm of establishing energy-exchange channels between photonic structures and the environment. For example, dissipationless photonic waveguide arrays[8,41] serve as unique platforms for observing the temporally unidirectional evolution of Hermitian topological states by using a specific waveguiding direction (e.g., $-z$ channel in **Figure 1**a) while not using the other direction ($+z$ channel). Passive-PT symmetries based on nonuniform loss (in Figure 1b) have been introduced into topological waveguide arrays to investigate the evolution of non-Hermitian topological states.[38,42] To date, the interplay between topological and non-Hermitian physics has not been realized in dissipationless photonic systems.

Beyond the paradigm discussed above, we here reveal the anti-parity-time (APT) symmetry in Hermitian valley photonic crystals (VPCs) and further harness it to realize an unusual

photonic topological device. By engineering the valley topologies in the VPCs, we designed two topological valley waveguides (TVWs) with group velocities in opposite directions. We theoretically reveal and experimentally demonstrate that the coupling between two TVWs renders an APT phase transition in the spectral domain, unlike conventional APT approaches that exploit dissipative/nonlinear processes.[12–32] In coupled topological valley waveguides (CTVWs), one waveguiding direction ($-z$ channel) works for the evolution of the topological modes, and the opposite direction ($+z$ channel), which is not utilized in conventional waveguide arrays, is used as an effective dissipation channel (as illustrated in Figure 1c). The valley topology protects the light propagations in both APT phases with near-vanished intervalley scattering from the joints between the CTVW and uncoupled TVWs. By further harnessing the effective dissipations with topological robustness and the near-vanished intervalley scattering property, we realize an unusual photonic topological bi-functional device that functions as a delay line and near-perfect absorber in different frequency regimes. All the above are experimentally demonstrated on silicon-on-insulator platforms at telecommunications wavelengths.

2. Results and Discussion

We first present a general theoretical analysis to elucidate the topology-spawned APT symmetry. The TVWs are constructed with two types of honeycomb lattices (HL1 and HL2), as depicted in Figure 1d. The two lattices are distinct in the locations of the two different atoms in each unit cell while sharing the same distance s between the two atoms. The tight-binding results (Section A, Supporting Information) show that both the lattices share the same dispersion bands, which exhibit energy minima (also termed valleys) at the Brillouin boundary. Band topology analysis (Section B, Supporting Information) discloses that the lattice distinctions lead to opposite valley Chern numbers at the same valley, for example, $C_{K,1} = -1/2$ and $C_{K,2} = 1/2$, where the subscript $K = \frac{2\pi}{3\sqrt{3}s}$ denotes the positive valley (Figure 1d). By connecting the two lattices, we constructed two different interfaces (HL1-HL2 and HL2-HL1), as shown in Figure 1d. By sufficiently separating the two interfaces transversely ($N \times 2s$, $N \in Z^+$, and $N>>1$), independent topological modes are waveguided along them while decaying along the transverse directions.

Due to the bulk-edge correspondence (Section C, Supporting Information), the upper and lower interfaces in Figure 1d host backward ($v_g \times v_p < 0$) and forward ($v_g \times v_p > 0$) waves, respectively (as shown in Figure 1e), where v_p and v_g represent the phase and group velocities, respectively. Taking the K valley as an example, where both interface modes exhibit positive phase velocities (in Figure 1e), the upper/lower interface mode, corresponding to a negative/positive topological invariant (i.e., $\Delta C_{K,u} = C_{K,1} - C_{K,2} = -1$, $\Delta C_{K,l} = C_{K,2} - C_{K,1} = 1$), shows a negative ($-v_g$)/positive ($v_g$) group velocity. This analysis is also applicable to the K' valley, where v_p and v_g reverse signs simultaneously. The upper and lower interfaces are also termed backward-wave and forward-wave topological valley waveguides (B-TVW and F-TVW), respectively. More specifically, the two TVWs follow linear dispersions expressed by $\omega_{F,B} - \omega_0 = \pm v_g(\beta_{F,B} - \beta_i)$ (Section C, Supporting Information), where (β_i, ω_0) is their intersection point in Figure 1e. Subscripts B and F denote backward and forward, respectively.

By setting a small separation (e.g., $N = 1$) between the two parallel TVWs in Figure 1d, they are evanescently coupled. Such a weak coupling only occurs between topological modes in the same valley because its perturbative nature cannot compensate for the very large wavevector detuning between different valleys. The CTVWs at the K valley are described using spatially coupled mode equations as

$$-i\frac{d}{dz}\begin{bmatrix} a_B \\ a_F \end{bmatrix} = \begin{bmatrix} \beta_B & \kappa_{BF} \\ \kappa_{FB} & \beta_F \end{bmatrix}\begin{bmatrix} a_B \\ a_F \end{bmatrix} = (\beta_i + \hat{H}_{eff})\begin{bmatrix} a_B \\ a_F \end{bmatrix} \quad (1)$$

In Equation (1), a_B and a_F represent the complex amplitude of the waves in the B-TVW and F-TVW, which share the same phase velocity directions but have opposite group velocity directions. To reveal the properties of the coupling coefficients κ_{BF} and κ_{FB}, we consider CTVWs as an effective continuous model, as shown in Figure 1c. Taking an arbitrary section in such a coupling configuration (Section D, Supporting Information), the opposite group velocities in the two waveguides transform the Hermitian (energy conservation) condition into an energy-flow-difference conservation $\frac{d}{dz}(|a_F(z)|^2 - |a_B(z)|^2) = 0$, which is consistent with the energy-difference conserving dynamics in electrical circuit resonators.[15] Substituting Equation (1) into the Hermitian condition, the coupling coefficients are obtained as purely imaginary numbers $\kappa_{FB} = \kappa_{BF} = i\kappa$ (Section D, Supporting Information). As the two TVWs are oppositely detuned by the same amount ($\beta_B = \beta_i - \Delta$, $\beta_F = \beta_i + \Delta$) (Figure 1e), the effective Hamiltonian of the CTVWs is expressed as

$$\hat{H}_{eff} = \begin{bmatrix} -\Delta & i\kappa \\ i\kappa & \Delta \end{bmatrix} \quad (2)$$

which is APT symmetric, i.e., $\{\hat{H}_{eff}, \hat{P}\hat{T}\} = 0$.

We further solve Equation (2) to elucidate the APT phase transition. The eigenvalues γ are obtained as

$$\gamma = \beta - \beta_i = \pm\sqrt{\Delta^2 - \kappa^2} \quad (3)$$

where β is the wavevector of the guided modes in the CTVWs. Sweeping the detuning Δ from the region $|\Delta| < |\kappa|$ to $|\Delta| > |\kappa|$, γ changes from a purely imaginary number to a purely real number (Figure 1f). This indicates that the CTVWs undergo spontaneous APT symmetry breaking and thus a phase transition. More specifically, regions $|\Delta| < |\kappa|$ and $|\Delta| > |\kappa|$ correspond to the APT-symmetric (APT-S) and APT-symmetry-broken (APT-B) phases, respectively. In addition, both the eigenvalues and eigenstates coalesce at the exceptional point $|\Delta| = |\kappa|$.

In turn, the topology-spawned APT symmetry changes the dispersions of the topological valley edge modes. Unlike changing structures in previously reported APT systems,[14,18,32] the wavevector detuning Δ in the CTVWs depends on the frequencies of edge modes, i.e., $\Delta = (\omega - \omega_0)/v_g$. By substituting the frequency-controlled detuning into Equation (3), we obtain the dispersion relation $(\omega - \omega_0)^2 = v_g^2\kappa^2 + v_g^2(\beta - \beta_i)^2$ of the CTVWs. As shown in Figure 1g, the dispersion of the CTVWs exhibits a forbidden band $|\omega - \omega_0| < |v_g\kappa|$ sandwiched between two allowed

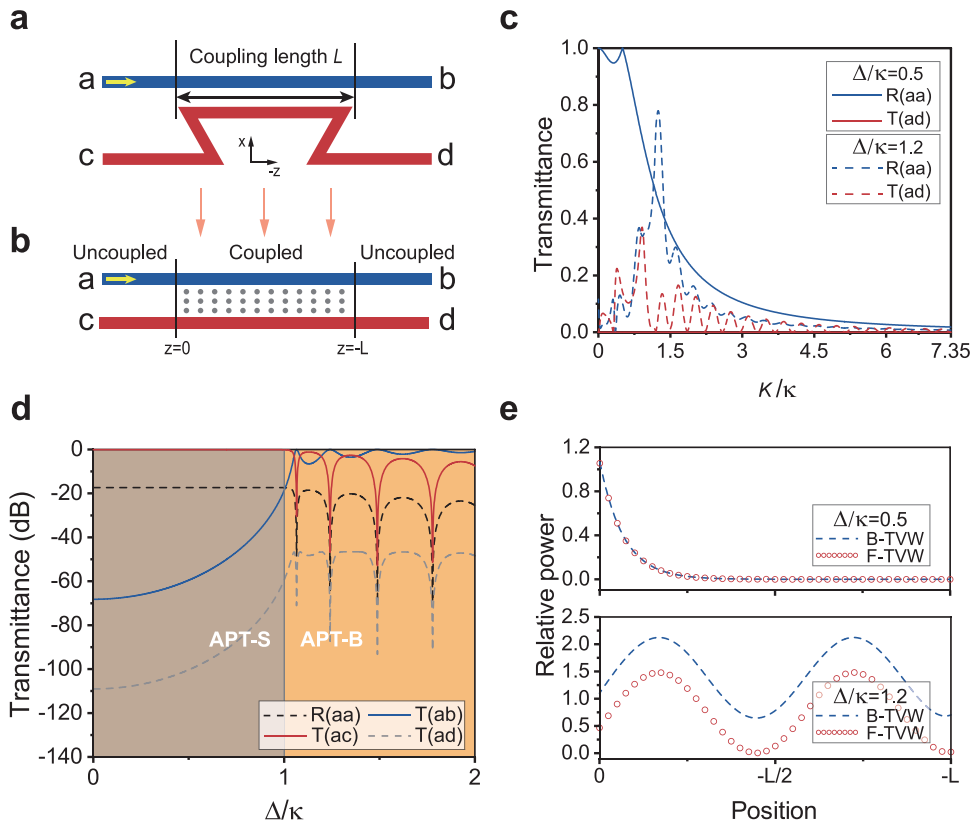

Figure 2. Light manipulation by the APT symmetry in finite CTVWs. a) Coupled straight-zigzag waveguides with coupling length L. The blue straight and red zigzag lines represent the B-TVW and F-TVW, respectively. b) Equivalent model of (a). c) Valley protection condition ($\beta_i >> \kappa$) in the CTVWs. The red and blue colors represent reflection to port a and transmission to port d, respectively. The solid and dashed lines indicate the APT-S and APT-B phases, respectively. d) Theoretical transmittance versus detuning Δ of the wavevectors. The transmittance spectra are obtained with $\kappa = 0.136\beta_i$ and $L = 8.541/\kappa$. The black line denotes the reflection to port a, and the blue, red, and gray lines indicate the transmittance of light from port a to ports b, c, and d, respectively. e) Power flows in the two waveguides for the APT-S ($\Delta/\kappa = 0.5$) and APT-B ($\Delta/\kappa = 1.2$) phases. The blue dashed and red circle lines indicate the power distributions in the B-TVW and F-TVW, respectively.

bands $|\omega - \omega_0| > |v_g\kappa|$. Therefore, the forbidden and allowed bands correspond to APT-S and APT-B phases, respectively.

Naturally, the two distinct APT phases of the CTVWs can manipulate the propagation of the topological valley edge modes in two distinct forms. We investigate the propagation properties by connecting finite CTVWs to uncoupled TVWs. As shown in **Figure 2**a, CTVWs of length L are constructed by coupling a section of a straight TVW with the top section of a zigzag TVW, whereas the other sections are uncoupled TVWs. Since the topological modes are insensitive to sharp bends,[43–46] this configuration is equivalent to a model (shown in Figure 2b) in which the finite CTVWs and uncoupled TVWs are directly connected. Inputting light from port a, the theoretical results in Figure 2c (Section E, Supporting Information) show that the reflection (R_{aa}) to port a and transmission (T_{ad}) to port d are near-zero in both phases in the weakly coupled region ($\beta_i >> \kappa$).Owing to the topological protection of valley edge states, β_i is stable at the valley K (or K'). The near-vanished R_{aa} and T_{ad} imply topologically prohibited intervalley scattering free from the joints between the CTVWs and uncoupled TVWs. Taking $\kappa = 0.136\beta_i$, we clearly identify two APT phases from both the transmission spectra in Figure 2d and the field distributions in Figure 2e. In the APT-S phase, the injected light is completely reflected to port c by the CTVWs (shown in Figure 2d), which is consistent with the evanescent fields in both the waveguides ($\Delta = 0.5\kappa$ in Figure 2e). In contrast, the APT-B phase hosts the propagating fields in the two waveguides ($\Delta = 1.2\kappa$ in Figure 2e) and allows a relatively high transmission to port b (shown in Figure 2d). Total transmission occurs at some specific detuning values in the APT-B phase owing to the L-dependent resonance transmission.

To demonstrate the above theoretical analysis, we fabricated samples using silicon-on-insulator platforms (see Experimental Section and Section L, Supporting Information). As shown in the scanning electron microscopy (SEM) image in **Figure 3**a, the sample contains valley photonic crystals composed of a honeycomb hole array with periodicity p = 401 nm and four single-mode silicon waveguides loaded with gratings at their ends for inputting or outputting light. The zoomed-in SEM image in Figure 3b shows a straight (backward) TVW and zigzag (forward) TVW separated by a distance of 462 nm in valley photonic crystals, with a coupling length L = 12.03 μm. The simulation results show that the dispersions of the uncoupled B-TVW (Figure 3c) and F-TVW reside in the bulk bandgap and intersect around the K point. Below the intersection point, the upper and lower interfaces exhibit nearly linear dispersions with negative and positive group velocities, respectively. Regarding

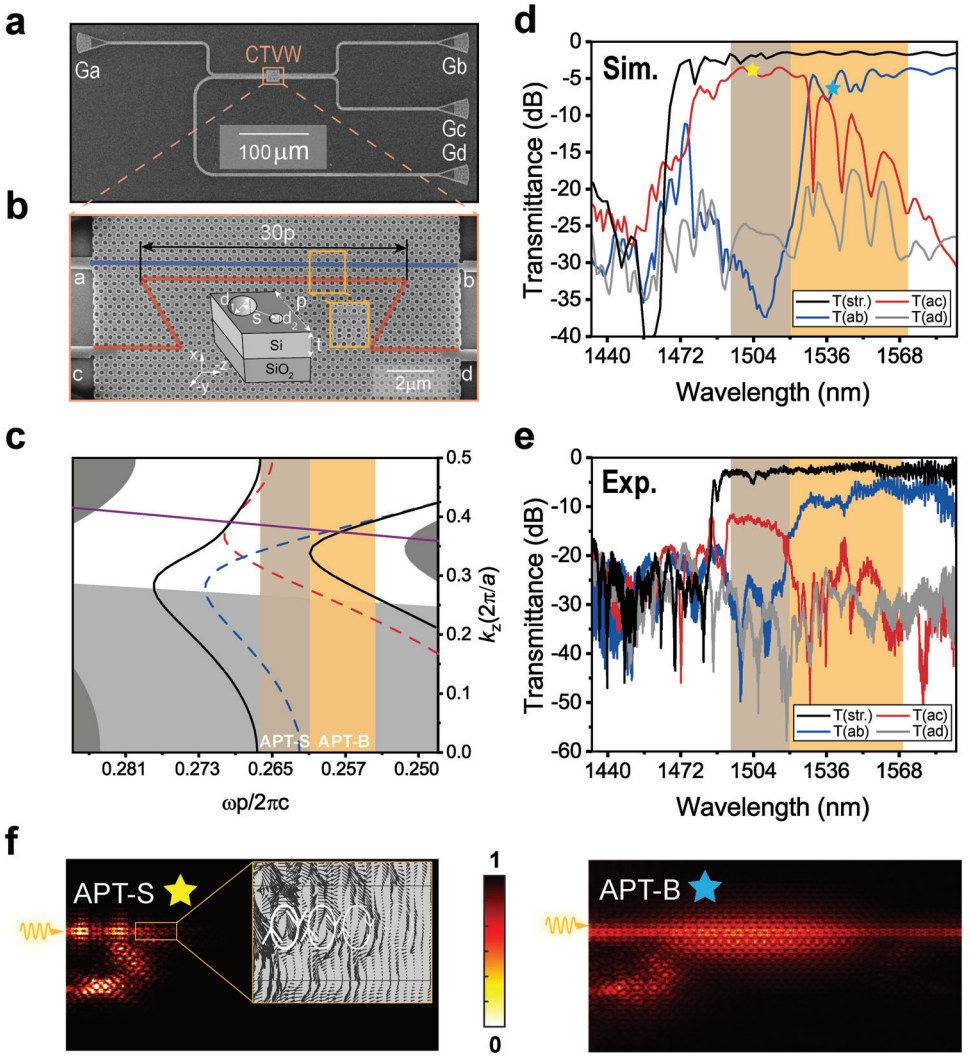

Figure 3. Observing APT phases in photonic CTVWs. a) SEM image of the fabricated sample, comprising CTVWs and four silicon waveguides coupled with gratings (Ga, Gb, Gc, and Gd). b) SEM image of the CTVWs. The right and left insets show a zoomed-in region and a unit cell, respectively. The silicon layer with a thickness of $t = 220$ nm is decorated with air holes in a honeycomb lattice. The periodicity is $p = 401$ nm. Holes with diameters of $d_1 = 174$ nm and $d_2 = 81$ nm are separated by $s = 231$ nm. The coupling length of the CTVWs is $30p$. c) Band diagrams of individual TVWs (red and blue dashed lines) and CTVWs (black solid lines). Brown region: APT-S band gap, orange region: APT-B edge dispersions, dark gray region: bulk states, gray region: above the air light line. The purple line indicates the silicon dioxide light line. d) Simulated and e) measured transmittance spectra through a straight TVW ($T_{str.}$) and CTVWs (T_{ab}, T_{ac}, and T_{ad}). f) Field patterns corresponding to the yellow and green stars in (d). The inset shows the simulated power flow of the APT-S phase.

the CTVWs (Figure 3b), a bandgap (indicated by the color brown in Figure 3c) emerges, corresponding to the APT-S phase. The coupling coefficient is estimated from the bandgap size as $\kappa = 0.136\beta_i$, which further confirms the valley protection. Each frequency in the edge band below the APT gap corresponds to two real wavevectors, thus manifesting the APT-B phase. Although the finite thickness of the sample results in radiation leakage into the substrate (topological edge dispersions lie above the light line of the silicon dioxide substrate), the simulated band diagram verifies our theoretical analysis of the 2D Hermitian systems.

We further conducted numerical (Figure 3d) and experimental (Figure 3e) spectral studies to verify the light manipulation capability of the two APT phases. Light was injected from port a and detected at ports b, c, and d. For reference, we first identified the topological valley edge-state band (1488–1580 nm) by measuring the transmission ($T_{str.}$ in Figure 3d,e) through a single straight TVW (Section F, Supporting Information). The propagation losses of the TVWs are estimated in Section G (Supporting Information). In further experiments (see Experimental Section; Section M, Supporting Information) on the CTVWs, we find that the input light in the 1492–1520 nm band cannot pass through the CTVWs but is totally reflected (effectively dissipated) to port c (T_{ac} in Figure 3e). The measured T_{ac} is in good agreement with the simulated spectrum in Figure 3d and the field pattern in Figure 3f, except for the lower amplitude, which is because of the enhanced radiation leakage induced by the roughness of the fabricated sample. The reflection is attributed to the closed loops of energy flows in each unit cell (Figure 3f), resulting from

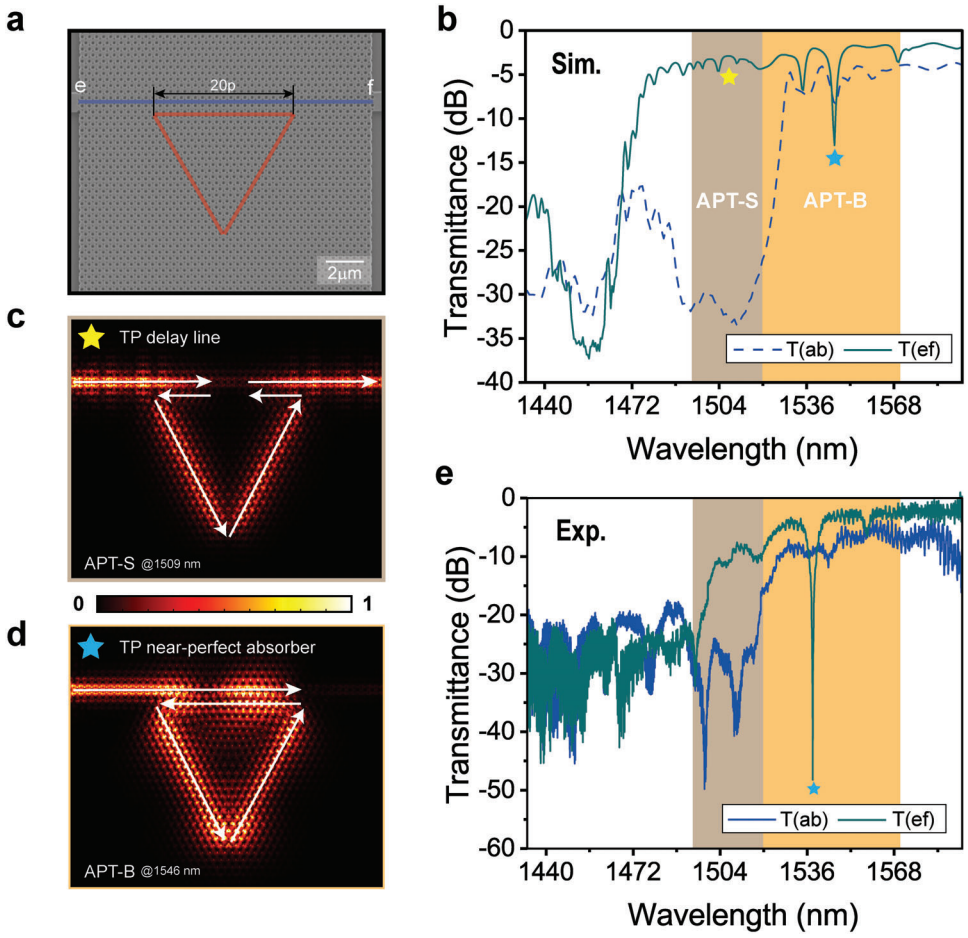

Figure 4. Topological APT photonic bi-functional device. a) SEM image of the photonic topological bi-functional device. The lengths of the coupled and uncoupled regions are 20*p*. b) Simulated transmittance spectra (T_{ef}) through the bi-functional device. Yellow and cyan stars indicate the delay line and on-chip absorber functions, respectively. c,d) Field patterns corresponding to the delay line and on-chip absorber functions, respectively. e) Measured transmittance spectra through the bi-functional device.

the coupling between the rightward and leftward energy flows in the B-TVW and the F-TVW. With respect to the normal input light, the reflected light is laterally shifted by such closed energy loops. The strength of these closed energy loops decays along the waveguide direction (Figure 3f), consistent with the theoretical results shown in Figure 2e. In contrast, the light in the rest of the edge-state band (1520–1593 nm) passes through the CTVWs and is partially transmitted as T_{ab} and partially reflected (effectively dissipated) as T_{ac} (in Figure 3d,e). The simulated field pattern in Figure 3f further verifies the light division, resulting from the two eigen wavevectors in the APT-B phase (Figure 1f). The roughness of the fabricated samples results in a lower T_{ac} than that in the simulation.

The effective dissipation (i.e., the reflected light) of the APT phases is further harnessed by exploiting the topological robustness and enables an unusual photonic topological bi-functional device, which is challenging to be realized in conventional contra-directional couplers.[47–51] We further close the zigzag waveguide and form a triangular-shaped topological resonator. The topological robustness ensures no reflection or localization by the sharp corners.[43–46] **Figure 4**a shows the SEM image of the bi-functional device, comprising a coupled topological waveguide resonator (CTWR) system. The upper edge of the triangular resonator is coupled with a straight topological waveguide and forms CTVWs, whereas the remaining two edges are uncoupled. Compared with the T_{ab} in the CTVWs (Figure 3d), the transmission (T_{ef}) through the CTWR exhibits distinct features in both the APT phases (Figure 4b). In the APT-S phase, the low-transmission band in the CTVWs disappears. The simulated field pattern (Figure 4c) clarifies that the injected light is reflected by the CTVW edge into the uncoupled edges and is further guided to port f (simulations for verifying the working mechanism of the delay line are shown in Section H, Supporting Information). Consequently, the CTWR in the APT-S phase functions as a delay line. Regarding the APT-B phase, a transmission dip (Q factor is ≈343.87, Section I, Supporting Information) emerges in T_{ef}. The field pattern in Figure 4d reveals that the CTVW edge splits the injected light into two parts that are separately guided through the CTVWs and uncoupled edges. Finally, the two parts destructively interfere at port f. According to the analysis shown in Figure 2c, the reflection to port e is near-zero. The simulation results also confirm the near-vanished

reflection (Section J, Supporting Information). Therefore, such a transmission dip in the APT-B phase indicates that the CTWR functions as a near-perfect absorber, in which light is consumed by radiation leakage. Notably, such an APT absorber lifts the critical requirements of the coherent injection of light as in coherent perfect absorbers.[52] The measured results in Figure 4e further demonstrate the functions of the photonic topological bi-functional device. Our photonic topological bi-functional device is based on the optical-routing capabilities of the frequency-domain APT phases of a fixed photonic platform, rather than on changing the photonic systems at different times.[36,53,54] Moreover, the temperature-dependent tunability of the permittivity of silicon provides an additional method for tuning the working wavelength of the topological near-perfect absorber mode of the CTWR. The evolution of the shifts in the transmission spectra upon heating the sample is shown in Section K (Supporting Information). Due to the intrinsic Kerr nonlinearity[55,56] of silicon, high-power inputs could also cause variations in the refractive index of silicon, thus providing another method to shift the working wavelength of the topological near-perfect absorber.

3. Conclusion

We realize APT symmetry in Hermitian CTVWs and observe the corresponding APT-symmetric and APT-symmetry-broken phases in the spectral domain. By combining the two phases and topological robustness, we realize a photonic topological bi-functional device that functions as a delay line and a near-perfect absorber in different frequency regions. Since the exceptional point of our system manifests zero group velocity (as shown in Figure 3c), which could decelerate the light and enhance the light-matter interactions,[55,56] our work provides easily-implementable platforms to study the quantum-exceptional-point resulted in intriguing phenomena.[57,58] Our platform could further interface with crystalline symmetries,[59] synthetic dimensions,[35,60] gain/dissipative media,[33–35,61] nonlinearity,[35,55,56] or quantum effects[62] and give rise to more intriguing non-Hermitian topological phenomena, nonlinear optics, or topological quantum optics. These findings may also be extended to other wave systems, such as acoustic or mechanical systems.

4. Experimental Section

Calculation and Simulation: COMSOL Multiphysics was used to obtain the band structures of the photonic crystals slab. Numerical transmission spectra and field patterns were obtained using the finite-difference time-domain method. The refractive index of silicon and silica were 3.47 and 1.45, respectively.

Design and Fabrication: The devices were fabricated on a standard silicon-on-insulator (SOI) wafer with a 220-nm-thick silicon layer on top of a 2-µm-thick buried oxide layer. The topological structures were patterned by electron beam lithography (Raith Voyager), employing positive-tone resist ARP. The patterns were then transferred from the photoresist to the silicon by inductively coupled plasma etching (Samco RIE-101iPH). Finally, the photoresist was removed by immersing the wafer into acetone for 30 min. Details of the fabrication process are shown in Figure S12 (Supporting Information).

Optical Measurements: The light source was a tunable laser (Santec TSL-550) covering a wavelength range from 1260 to 1620 nm. The light was coupled in and out of the device-under-test (DUT) through grating couplers by single-mode optical fibers and then collected using an optical power meter (MPM-210). The transmission was optimized by tuning the polarization of the light launched into the waveguide through a fiber-based polarization controller. Details of the measurement setup can be found in Figure S13 (Supporting Information).

Supporting Information

Supporting Information is available from the Wiley Online Library or from the author.

Acknowledgements

X.X., M.W., and Y.Y. contributed equally to this work. This work was supported by the National Key Research and Development Program of China under Grants no. 2022YFA1404902, 2022YFA1404704, 2022YFA1405200 and 2019YFB2203002, the National Natural Science Foundation of China (NNSFC) under grant no. 62171406, 11961141010, 61975176, 91950204, 61975177, and U20A20164, the Zhejiang Provincial Natural Science Foundation under grants no. Z20F010018, the Key Research and Development Program of Zhejiang Province under grant no. 2022C01036, and the Fundamental Research Funds for the Central Universities.

Conflict of Interest

The authors declare no conflict of interest.

Data Availability Statement

The data that support the findings of this study are available from the corresponding author upon reasonable request.

Keywords

anti-parity-time symmetry, phase transitions, silicon on insulators, topological edge states, valley photonic crystals

Received: February 25, 2023
Revised: April 19, 2023
Published online: June 4, 2023

[1] M. Z. Hasan, C. L. Kane, *Rev. Mod. Phys.* **2010**, *82*, 3045.
[2] F. D. M. Haldane, S. Raghu, *Phys. Rev. Lett.* **2008**, *100*, 013904.
[3] Z. Wang, Y. Chong, J. D. Joannopoulos, M. Soljačić, *Nature* **2009**, *461*, 772.
[4] K. G. Makris, R. El-Ganainy, D. N. Christodoulides, Z. H. Musslimani, *Phys. Rev. Lett.* **2008**, *100*, 103904.
[5] T. Ozawa, H. M. Price, A. Amo, N. Goldman, M. Hafezi, L. Lu, M. C. Rechtsman, D. Schuster, J. Simon, O. Zilberberg, I. Carusotto, *Rev. Mod. Phys.* **2018**, *91*, 015006.
[6] R. El-Ganainy, K. G. Makris, M. Khajavikhan, Z. H. Musslimani, S. Rotter, D. N. Christodoulides, *Nat. Phys.* **2018**, *14*, 11.
[7] Ş. K. Özdemir, S. Rotter, F. Nori, L. Yang, *Nat. Mater.* **2019**, *18*, 783.
[8] M. C. Rechtsman, J. M. Zeuner, Y. Plotnik, Y. Lumer, D. Podolsky, F. Dreisow, S. Nolte, M. Segev, A. Szameit, *Nature* **2013**, *496*, 196.
[9] M. Hafezi, S. Mittal, J. Fan, A. Migdall, J. M. Taylor, *Nat. Photonics* **2013**, *7*, 1001.

[10] A. B. Khanikaev, S. Hossein Mousavi, W.-K. Tse, M. Kargarian, A. H. MacDonald, G. Shvets, *Nat. Mater.* **2013**, *12*, 233.
[11] W.-J. Chen, S.-J. Jiang, X.-D. Chen, B. Zhu, L. Zhou, J.-W. Dong, C. T. Chan, *Nat. Commun.* **2014**, *5*, 5782.
[12] L. Ge, H. E. Türeci, *Phys. Rev. A* **2013**, *88*, 053810.
[13] P. Peng, W. Cao, C. Shen, W. Qu, J. Wen, L. Jiang, Y. Xiao, *Nat. Phys.* **2016**, *12*, 1139.
[14] F. Yang, Y.-C. Liu, L. You, *Phys. Rev. A* **2017**, *96*, 053845.
[15] Y. Choi, C. Hahn, J. W. Yoon, S. H. Song, *Nat. Commun.* **2018**, *9*, 2182.
[16] Y. Li, Y. Peng, L. Han, M.-A. Miri, W. Li, M. Xiao, X.-F. Zhu, J. Zhao, A. Alù, S. Fan, C.-W. Qiu, *Science* **2019**, *364*, 170.
[17] Y.-H. Lai, Y.-K. Lu, M.-G. Suh, Z. Yuan, K. Vahala, *Nature* **2019**, *576*, 65.
[18] X.-L. Zhang, T. Jiang, C. T. Chan, *Light: Sci. Appl.* **2019**, *8*, 88.
[19] F. Zhang, Y. Feng, X. Chen, L. Ge, W. Wan, *Phys. Rev. Lett.* **2019**, *124*, 053901.
[20] M. De Carlo, F. De Leonardis, L. Lamberti, V. M. N. Passaro, *Opt. Lett.* **2019**, *44*, 3956.
[21] Y. Jiang, Y. Mei, Y. Zuo, Y. Zhai, J. Li, J. Wen, S. Du, *Phys. Rev. Lett.* **2019**, *123*, 193604.
[22] H. Zhang, R. Huang, S.-D. Zhang, Y. Li, C.-W. Qiu, F. Nori, H. Jing, *Nano Lett.* **2020**, *20*, 7594.
[23] W. Cao, X. Lu, X. Meng, J. Sun, H. Shen, Y. Xiao, *Phys. Rev. Lett.* **2020**, *124*, 030401.
[24] F. Wang, X. Niu, X. Hu, T. Gu, X. Wang, J. Yang, H. Yang, Y. Ao, S. Wang, Q. Gong, *Phys. Rev. Appl.* **2020**, *14*, 044050.
[25] J. Wen, G. Qin, C. Zheng, S. Wei, X. Kong, T. Xin, G. Long, *npj Quantum Inf.* **2020**, *6*, 28.
[26] J. M. P. Nair, D. Mukhopadhyay, G. S. Agarwal, *Phys. Rev. Lett.* **2021**, *126*, 180401.
[27] A. Bergman, R. Duggan, K. Sharma, M. Tur, A. Zadok, A. Alù, *Nat. Commun.* **2021**, *12*, 486.
[28] H. Zhang, M. Peng, X.-W. Xu, H. Jing, *Chin. Phys. B* **2022**, *31*, 014215.
[29] Y. Yang, X. Xie, Y. Li, Z. Zhang, Y. Peng, C. Wang, E. Li, Y. Li, H. Chen, F. Gao, *Nat. Commun.* **2022**, *13*, 7678.
[30] L. Ding, K. Shi, Y. Wang, Q. Zhang, C. Zhu, L. Zhang, J. Yi, S. Zhang, X. Zhang, W. Zhang, *Phys. Rev. A* **2022**, *105*, L010204.
[31] Y. He, J. Wu, Y. Hu, J.-X. Zhang, S.-Y. Zhu, *Phys. Rev. A* **2022**, *105*, 043712.
[32] W. Liu, Y. Zhang, Z. Deng, J. Ye, K. Wang, B. Wang, D. Gao, P. Lu, *Laser Photonics Rev.* **2022**, *16*, 2100675.
[33] E. J. Bergholtz, J. C. Budich, F. K. Kunst, *Rev. Mod. Phys.* **2021**, *93*, 015005.
[34] C. Coulais, R. Fleury, J. van Wezel, *Nat. Phys.* **2021**, *17*, 9.
[35] H. Price, Y. Chong, A. Khanikaev, H. Schomerus, L. J. Maczewsky, M. Kremer, M. Heinrich, A. Szameit, O. Zilberberg, Y. Yang, B. Zhang, A. Alù, R. Thomale, I. Carusotto, P. St-Jean, A. Amo, A. Dutt, L. Yuan, S. Fan, X. Yin, C. Peng, T. Ozawa, A. Blanco-Redondo, *J. Phys. Photonics* **2022**, *4*, 032501.
[36] H. Zhao, X. Qiao, T. Wu, B. Midya, S. Longhi, L. Feng, *Science* **2019**, *365*, 1163.
[37] S. Weidemann, M. Kremer, T. Helbig, T. Hofmann, A. Stegmaier, M. Greiter, R. Thomale, A. Szameit, *Science* **2020**, *368*, 311.
[38] S. Xia, D. Kaltsas, D. Song, I. Komis, J. Xu, A. Szameit, H. Buljan, K. G. Makris, Z. Chen, *Science* **2021**, *372*, 72.
[39] P. St-Jean, V. Goblot, E. Galopin, A. Lemaître, T. Ozawa, L. L.e Gratiet, I. Sagnes, J. Bloch, A. Amo, *Nat. Photonics* **2017**, *11*, 651.
[40] M. A. Bandres, S. Wittek, G. Harari, M. Parto, J. Ren, M. Segev, D. N. Christodoulides, M. Khajavikhan, *Science* **2018**, *359*, eaar4005.
[41] N. Malkova, I. Hromada, X. Wang, G. Bryant, Z. Chen, *Opt. Lett.* **2009**, *34*, 1633.
[42] S. Weimann, M. Kremer, Y. Plotnik, Y. Lumer, S. Nolte, K. G. Makris, M. Segev, M. C. Rechtsman, A. Szameit, *Nat. Mater.* **2017**, *16*, 433.
[43] F. Gao, H. Xue, Z. Yang, K. Lai, Y. Yu, X. Lin, Y. Chong, G. Shvets, B. Zhang, *Nat. Phys.* **2018**, *14*, 140.
[44] X.-T. He, E.-T. Liang, J.-J. Yuan, H.-Y. Qiu, X.-D. Chen, F.-L. Zhao, J.-W. Dong, *Nat. Commun.* **2019**, *10*, 872.
[45] M. I. Shalaev, W. Walasik, A. Tsukernik, Y. Xu, N. M. Litchinitser, *Nat. Nanotechnol.* **2019**, *14*, 31.
[46] Z. Zhang, Y. Li, C. Wang, S. Xu, Z. Wang, E. Li, H. Chen, F. Gao, *Appl. Phys. Lett.* **2022**, *121*, 011701.
[47] M. Qiu, M. Mulot, M. Swillo, S. Anand, B. Jaskorzynska, A. Karlsson, M. Kamp, A. Forchel, *Appl. Phys. Lett.* **2003**, *83*, 5121.
[48] H. Qiu, H. Yu, T. Hu, G. Jiang, H. Shao, P. Yu, J. Yang, X. Jiang, *Opt. Express* **2013**, *21*, 17904.
[49] M. G. Scullion, A. Di Falco, T. F. Krauss, *Opt. Lett.* **2014**, *39*, 4345.
[50] D. Oser, F. Mazeas, X. L.e Roux, D. Pérez-Galacho, O. Alibart, S. Tanzilli, L. Labonté, D. Marris-Morini, L. Vivien, É. Cassan, C. Alonso-Ramos, *Laser Photonics Rev.* **2019**, *13*, 1800226.
[51] M. Minz, R. K. Sonkar, *Appl. Opt.* **2021**, *60*, 2640.
[52] D. G. Baranov, A. Krasnok, T. Shegai, A. Alù, Y. Chong, *Nat. Rev. Mater.* **2017**, *2*, 17064.
[53] J. W. You, Q. Ma, Z. Lan, Q. Xiao, N. C. Panoiu, T. J. Cui, *Nat. Commun.* **2021**, *12*, 5468.
[54] H. Wang, G. Tang, Y. He, Z. Wang, X. Li, L. Sun, Y. Zhang, L. Yuan, J. Dong, Y. Su, *Light: Sci. Appl.* **2022**, *11*, 292.
[55] J. Leuthold, C. Koos, W. Freude, *Nat. Photonics* **2010**, *4*, 535.
[56] D. Smirnova, D. Leykam, Y. Chong, Y. Kivshar, *Appl. Phys. Rev.* **2020**, *7*, 021306.
[57] F. Minganti, A. Miranowicz, R. W. Chhajlany, F. Nori, *Phys. Rev. A* **2019**, *100*, 062131.
[58] R. Huang, Ş. K. Özdemir, J.-Q. Liao, F. Minganti, L.-M. Kuang, F. Nori, H. Jing, *Laser Photonics Rev.* **2022**, *16*, 2100430.
[59] H. Xue, Y. Yang, F. Gao, Y. Chong, B. Zhang, *Nat. Mater.* **2019**, *18*, 108.
[60] A. Dutt, Q. Lin, L. Yuan, M. Minkov, M. Xiao, S. Fan, *Science* **2020**, *367*, 59.
[61] Y. Zeng, U. Chattopadhyay, B. Zhu, B. Qiang, J. Li, Y. Jin, L. Li, A. G. Davies, E. H. Linfield, B. Zhang, Y. Chong, Q. J. Wang, *Nature* **2020**, *578*, 246.
[62] P. Lodahl, S. Mahmoodian, S. Stobbe, A. Rauschenbeutel, P. Schneeweiss, J. Volz, H. Pichler, P. Zoller, *Nature* **2017**, *541*, 473.